Symmetric Instability in the Outflow Layer of a Major Hurricane

John Molinari and David Vollaro

Department of Atmospheric and Environmental Sciences, University at Albany,

State University of New York, Albany, New York

Journal of the Atmospheric Sciences

Accepted July 15, 2014

Corresponding author address:
John Molinari
University at Albany, SUNY
Atmospheric and Environmental Sciences, ES 351
1400 Washington Avenue
Albany, NY 12222

ABSTRACT

A set of 327 dropsondes from the NOAA G-IV aircraft was used to create a composite analysis of the azimuthally-averaged absolute angular momentum in the outflow layer of major Hurricane Ivan (2004). Inertial instability existed over a narrow layer in the upper troposphere between the 350 and 450 km radii. Isolines of potential and equivalent potential temperature showed that the conditions for both dry and moist symmetric instability were satisfied in the same region, but over a deeper layer from 9-12 km. The radial flow maximized at the outer edge of the unstable region. The symmetrically unstable state existed above a region of outward decrease of temperature between the cirrus overcast of the storm and clear air outside. It is hypothesized that the temperature gradient was created as a result of longwave heating within the cirrus overcast and longwave cooling outside the cloudy region. This produced isentropes that sloped upward with radius in the same region that absolute momentum surfaces were flat or sloping downward, thus creating symmetric instability. Although this instability typically follows rather than precedes intensification, limited numerical evidence suggests that the re-establishment of a symmetrically neutral state might influence the length of the intensification period.

1. Introduction

The potential importance of outflow layer inertial instability in tropical cyclone formation and intensification has been addressed for many years (see review by Yanai 1964). Sawyer (1947) argued that negative absolute vorticity within the outflow layer, possibly associated with cumulus convection in a precursor disturbance, would produce divergent outflow in the upper troposphere that might further organize core convection and thus lead to intensification. Alaka (1962) and Black and Anthes (1971) provided evidence that local regions of inertial instability exist within tropical cyclone outflow.

Kleinschmidt (1951) made similar arguments to Sawyer (1947), but examined inertial stability along vertically sloping equivalent potential temperature (θ_e) surfaces, a measure of (moist) symmetric instability. This instability exists in tropical cyclones if the radial slope of the θ_e surface exceeds that of the M surface (e.g., Fig. 18 of Yanai 1964). Ooyama (1966) noted that such flow is unstable to displacements in both radial directions, but if the mean flow is outward then the acceleration would be expected to be outward, within the constraints of mass conservation.

The arguments that inertial and/or symmetric instabilities feed back to produce intensification of tropical cyclones were physically appealing, but in early numerical simulations of tropical cyclones, Ooyama (1969) and Anthes (1972) found that inertial instability *followed* rather than preceded intensification. As a result, interest in this instability and its potential role in tropical cyclones nearly vanished for many years. Möller and Shapiro (2002) and Bui et al. (2009) found small regions of symmetric instability in the mature tropical cyclone outflow layer, expressed by an ellipticity condition for a second order balanced vortex equation not being met, but the instabilities were examined only in terms of their being an obstacle to solution of the

equations. Rappin et al. (2011) investigated the role of varying background rotation on tropical cyclone intensification, but did not address a possible role for symmetric instability.

In this paper the existence of such instability will be described in major Hurricane Ivan (2004). The means of generation of inertial and symmetric instabilities and their possible roles in the structure and intensity of the storm will be addressed.

2. Data and Methods

The data for this study comprise 327 GPS sondes (Hock and Franklin 1999) released in Hurricane Ivan by the NOAA G-IV aircraft. They covered the period 6-16 September, as the storm moved from near 10°N, 50°W to the central Gulf of Mexico. For all but 12 hours of the sonde collection, Ivan was a major hurricane with maximum winds exceeding 110 kt (57 m s^{-1}). The history of Hurricane Ivan is described by Franklin et al. (2006).

The sondes were processed following Molinari et al. (2012) and Molinari et al. (2014). The average sonde release level was near 13 km. The data were interpolated to 100-m vertical resolution within 100-km radial bins. For convenience, the radial bins will be identified by their midpoint, i.e., the 100-200 km bin will be labeled as the 150 km radius. All analyses will be shown in radius-height (r-z) sections. Each plot will display an average value of all sondes within the radius bin at each level. Owing to the extremely high vertical resolution combined with relatively coarse horizontal resolution, a 1-2-1 smoother was applied five times in the vertical in all r-z cross-sections.

The radius of each sonde was determined by the great circle distance from the storm center. The latter was defined using the Best Track data from the National Hurricane Center, linearly interpolated to one-minute positions. This high time resolution of the track allowed the sonde radius to be determined at each level, i.e., the drift of the sonde was accounted for. In

reality, of course, the storm does not move linearly between the 6-h Best Track positions. Rather, the one-minute interpolation prevented artificial jumps in sonde positions during their descent.

The distribution of sonde release locations with respect to the center of the storm is given in Fig. 1. The distribution is reasonably uniform in radius and azimuth except in three regions. Only a single sonde was released within the 100 km radius, and that region will be omitted. Few sondes were released north of the storm between the storm center and the 250 km radius, and south of the center outside of the 600-km radius. In order to investigate the impact of these data-sparse regions, azimuthally-averaged absolute angular momentum was calculated, given by

$$M = rv_{\lambda} + \frac{fr^2}{2} \qquad (1)$$

where v_{λ} is storm-relative tangential velocity. Fig. 2 shows a radius-height (r-z) composite of this field with 100-km radial spacing and 100-m vertical spacing as noted above. The stippling shows regions in which *M* decreased outward on geopotential height surfaces. The *M* fields exhibited a smaller outward slope in the lower and middle troposphere than in the upper troposphere, consistent with smaller vertical shear of the tangential wind in this region. The *M* surfaces bowed outward in the upper troposphere, reflecting the development of anticyclonic flow at larger radii. To the authors' knowledge, no examples of the observed *M* distribution on the scale of Fig. 2 are available in the published literature. We have obtained *M* cross-sections that extend beyond the 400-km radius from real-data simulations carried out by Nolan et al. (2013), Chen and Zhang (2012), and Huang et al. (2012). The *M* distribution in Fig. 2 resembles those provided by these authors within 550 km of the center, including a region of outward decrease of *M* in the first two of those papers. The focus of this paper will be on the decrease of *M* with radius between 350 and 450 km in Fig. 2 and related inertial and symmetric instabilities. Fig. 1 indicated that the data coverage and uniformity in that radial region were reasonably good. The missing data north of

the storm inside r = 300 km is not within this region of interest and thus should not have a major influence on the conclusions of this paper.

Fig. 2 also reveals an inertial wall (a strong outward increase in M) from 7-11 km height at r = 600 km. Over the next 100 km, M was nearly constant with radius in the upper troposphere. At these large radii, neither of these characteristics seems consistent with any physical process. M values calculated using gridded analyses from the European Center for Medium Range Weather Forecasting (ECMWF; not shown) indicated minima in the upper troposphere south of the center outside the 600 km radius, a region with a dearth of data (Fig. 1). It is possible that the inertial wall was an artifact that resulted from the discontinuity in data density. As a result, subsequent analyses will show only from the 150 km to the 550 km radii. The 550 km radius encompassed most of the region of cyclonic flow within the storm as well as the full structure of the central overcast (see Figs. 3-4). In order to focus on the outflow layer, only the levels from 7-13 km are displayed.

A second potential source of error could arise from an uneven distribution of sondes with time. The mean sonde release time and its standard deviation are given in Table 1 for each radial bin. Although the data were collected over 10 days, the mean times at adjacent radii fell in the middle of the period at all radii of interest, with no more than 18 hours time difference. In addition, the standard deviation was virtually identical at all radii, indicating a relatively uniform spread of observations in time. The number of sondes peaked at the radii of greatest interest. Fig.1 and Table 1 suggest that the spatial and temporal distribution of sondes should not significantly bias the results. Subsequent r-z sections are interpreted as azimuthal mean fields over the life of Hurricane Ivan. No steady-state assumption is required. This issue will be addressed further in the Discussion.

3. Results

a. Observations

The mean storm-relative radial velocity field in Hurricane Ivan (Fig. 3a) reveals maximum outflow exceeding 8 m s^{-1} at the 12-km level and the 550 km radius. Outflow increased with radius from r = 250 km to the edge of the figure over a layer from 10-13 km. The variation was even stronger with respect to mass flux (not shown); the outward flux at the 12 km level at 550 km radius was eight times that at 250 km. Outflow increased with height outside the 250 km radius above the 9-km level. Points A and A' in Fig. 3a will be discussed with subsequent figures. Storm-relative tangential velocity (Fig. 3b) revealed deep cyclonic flow. Anticyclonic flow existed in the upper troposphere outside of the 450 km radius.

The same *M* cross-section as in Fig. 2 is plotted with the mean relative humidity in Hurricane Ivan in Fig. 4. Relative humidity was calculated with respect to ice at temperatures below 0°C and with respect to water otherwise. The edge of the cirrus overcast in the composite was identified by the 80% contour in relative humidity. The central overcast extended outward to beyond the 350 km radius between 10.2 and 11.6 km heights. This relative humidity contour provides only an approximation of the cloud edge. In particular, the known dry bias in these dropsondes at low temperatures (see Appendix from Molinari et al. 2014) makes the upper limit of the overcast uncertain. Cairo et al. (2008) found the cirrus overcast in a tropical cyclone extended all the way to the tropopause, and it seems likely this would hold in a tropical cyclone as intense as Hurricane Ivan. As a result, the relative humidity below 80% at upper levels in Fig. 4 does not preclude the central overcast having reached those levels.

The almost constant *M* field with radius above the 12.5 km level from 250-350 km radii in Fig. 4 represented near neutral inertial stability. The *M* surfaces sloped downward from 350-450

km radii between the 10.7 and 12.2 km levels, indicating inertial instability (e.g., Kepert 2010). The unstable layer was present near the outer edges of the central cloud cover.

The same M contours are shown in Fig. 5a, this time superimposed over equivalent potential temperature (θ_e). Although the M surfaces sloped downward with radius near the edge of the central cloud cover, the θ_e surfaces retained an upward slope. This distribution of M and θ_e represents moist symmetric instability (e.g., Emanuel 1983). When θ_e increases upward and M decreases upward, this condition can be expressed by:

$$\left.\frac{\partial z}{\partial r}\right|_{\theta_e} > \left.\frac{\partial z}{\partial r}\right|_{M} \qquad (2)$$

indicating that the azimuthally-averaged θ_e surfaces slope upward with radius more than the M surfaces (Yanai 1964). Moist symmetric instability (shading in Fig. 5a) existed at the same radius as inertial instability, but through a deeper layer. The consequences of this deep layer of instability can be seen by tracing flow from point A in Fig. 5a. An axisymmetric tube of air moving outward while conserving θ_e (i.e., moving along the θ_e surface passing through A) would possess M larger than its environment and accelerate outward (see similar arguments by Emanuel 1983 and Thorpe et al. 1989). It is apparent from the figure that this acceleration would continue beyond the edge of the plot near the 11-km level, because the parcel would not yet have returned to its original M surface. The impact of the unstable region thus extends beyond the radius where the condition in Eq. 2 is met. Consistent with these arguments, the radial velocity (Fig. 3a) increased outward within the unstable region to a maximum at the 550 km radius. Figs. 4-5 suggest that the magnitude and structure of the outflow were connected to the presence of this instability.

An additional symmetrically unstable area in Fig. 5a was located above the 12-km level in the storm core where the flow was close to inertially neutral (nearly flat M surfaces). The instability arose because the θ_e surfaces sloped upward in the presence of a radial temperature gradient associated with the warm core. The radial velocity also accelerated outward in this region (Fig. 3a), supporting the hypothesis that symmetric instability was influencing the outflow structure of the storm over a fairly deep layer.

The use of θ_e in Fig 5a implies saturation during some part of the process. The mean relative humidity (Fig. 4) decreased with radius, and most likely a mix of saturated and unsaturated air existed outside the 350 km radius. Fig. 5b substitutes virtual potential temperature θ_v for θ_e in order to identify dry symmetric instability. The layer of such instability narrowed in the vertical compared to Fig. 5a. For instance, air carried outward on an isentropic surface through point B reveals only weak instability compared to Fig. 5a. Below point B was a nearly symmetrically-neutral layer at a location that was strongly unstable in Fig. 5a. Fig. 3a showed that radial velocity increased outward only above the 10.5 km height. As a result, the dry symmetric instability field, which indicated only small or no instability below 10 km, might have been most relevant in shaping the outflow distribution at these larger radii, where saturation was more intermittent than in the storm core.

b. Numerical modeling example

The greatest uncertainty in Figs. 4-5 is the assumption that the composite structure of 327 sondes over 10 days represents a realizable time- and azimuthally-averaged state. Evidence was provided in Fig. 1 and Table 1 that the spatial and temporal distribution of data did not bias the analysis over the 350-550 km radii of primary interest. In this section, a similar symmetrically unstable structure will be shown from the high-resolution numerical modeling study of Nolan et

al. (2013). This model contained 1-km inner grid spacing, double-moment microphysics, and cloud-radiative interaction with the radiation parameterization called every 6 minutes. It contained 60 vertical levels, including 8 levels between 9 and 13 km height. This model thus provided physical parameterizations that effectively simulated the diabatic physics of the central cloud mass of the tropical cyclone. Additional details are provided by Nolan et al. (2013).

Cross-sections of M (black contours) and θ_e (shaded) from the Nolan et al. (2013) simulation are shown in Fig. 6. The region of inertial instability in the simulation closely overlapped that of symmetric instability, and only the former is shaded in Fig. 6. The plots extend 3 km higher than Fig. 5. Fig. 6a represents a single time during the simulation. Instability existed from the 200 to 500 km radii between 12.5 and 14 km elevation. Nolan et al. (2013; their Figs. 4 and 17a) showed that Fig. 6a was valid during, rather than prior to, a time of rapid intensification. This is consistent with the arguments of Anthes (1972) and Ooyama (1969) that instability followed rather than led significant intensification. This instability relaxed back to a nearly neutral state after 6-8 hours (not shown). Rapid intensification ended in the model at about the same time, suggesting that the creation and removal of symmetric instability might have played a role in the length of the rapid intensification period.

The same fields are displayed in Fig. 6b, but averaged over a 48-hour period that included the times of rapid intensification. This time average still contained an inertially and symmetrically unstable state. The instability existed outside the model CDO as defined by the relative humidity (not shown), consistent with the structures shown earlier for Hurricane Ivan. Fig. 6 provides numerical modeling support for the observed instability shown in Figs. 4-5.

4. Discussion

Symmetric instability in Hurricane Ivan (2004) occurred over a wider region than inertial instability. One symmetrically unstable region existed above the 12-km level inside the 450 km radius. This area was characterized by nearly flat M surfaces with radius in the presence of sloping θ_v and θ_e surfaces. This unstable region could be produced by near-zero potential vorticity air from central convection in the presence of a radial temperature gradient associated with the warm core. One might expect such an unstable region to develop with every substantial burst of convection in the storm. The observed outflow in Hurricane Ivan increased outward in this region, suggesting that such instability was frequently active.

A second unstable region existed near the edge of the central cirrus overcast of the storm at the 350 – 450 km radii. Moist symmetric instability existed in this region over a deep layer from 7.5 – 12 km height. Dry symmetric instability was restricted more to the upper troposphere. Rings of air following isentropic surfaces would be accelerated outward beyond the 550 km radius by the symmetric instability. The mean outflow showed outward acceleration in this region.

It seems counterintuitive that a mean state should be unstable. In Hurricane Ivan, one half of the six-hour G-IV observation periods (7 of 14) experienced $\geq$ 5 hPa $(6\ h)^{-1}$ deepening, and these were distributed throughout the 10 days of observation. At least one eyewall replacement cycle occurred during the 10-day period of data collection (Sitkowski et al. 2011). If unstable states developed during these deepening periods, the subsequent response would produce a return to nearly neutral stability, but no further. The average state would be weakly unstable, consistent with Figs 4, 5, and 6b. For this reason, the use of composite fields in Figs. 4 and 5

does not indicate an assumption of a steady-state storm. Rather, the mean state shown in these figures represents the sum of unstable and neutral states.

The inertial instability near the edge of the central overcast arose because the *M* surfaces sloped downward with radius. The radial-vertical circulation of the storm, with upward motion in the core and compensating subsidence outside the central overcast, could have produced such an *M* distribution. But the θ_e surfaces should have turned downward by the same process. The fact that they do not is what created the symmetric instability. The reasons for this behavior might resemble those in the Hadley Cell circulation (Tim Dunkerton, personal communication, 2013). Near-zero potential vorticity upper-tropospheric air emitted from tropical convection produces nearly flat *M* surfaces on the poleward side. As this air continues poleward in the return branch of the Hadley Cell it eventually subsides and the *M* surfaces turn downward, creating inertial instability (see discussion by Sato and Dunkerton 2002). Wirth and Dunkerton (2006) introduced a soft inertial adjustment (and thus an implied momentum source) to allow parcels to cross *M* surfaces. This simulated the removal of such inertial instability by small-scale motions. In Hadley Cell theory, radiative cooling prevents the isentropes from turning downward as much as the *M* surfaces, thus creating symmetric instability (Held and Hou 1980). Held and Hou noted that this instability can co-exist with a steady Hadley Circulation.

Diabatic processes might also help to create the symmetric instability in tropical cyclones. Examination of Fig. 5a shows that radially inside point A, the slope of the θ_e surfaces with radius was small, whereas outside point A the slope increased. Fig. 4 shows that point A lies near the edge of the cloudy region. The smaller radial potential temperature gradient is consistent with longwave warming that would be expected within the cirrus overcast (Bu et al. 2014; Melhauser and Zhang 2014), which would slow the general decrease of temperature with radius in the

warm-core disturbance. Longwave cooling outside the cirrus overcast at the same levels would then locally enhance the radial temperature gradient and turn the isentropes upward with radius. In terms of thermal wind reasoning, the radial temperature gradient created an upward decrease in tangential wind near the edge of the clouds. The weaker tangential flow with radius in that layer would locally reduce *M*, consistent with the structure shown in Figs. 4-5. The net impact of the radial gradient in longwave heating would be to turn the isentropes upward in the same region that the *M* surfaces are flat or sloping downward, thus creating symmetric instability. It is proposed that diabatic physics might play a significant role in helping to create these dynamical instabilities.

Previous studies by Ooyama (1969) and Anthes (1972), as well as the simulation of Nolan et al. (2013), show that symmetric instability does not appear to initiate rapid intensification in tropical cyclones. The Nolan et al. (2013) results, however, suggested that the process by which symmetric instability is *removed* might play a key role in the nature and even the length of periods of rapid intensification. As a result, study of both the generation and the removal of symmetric instability in high-resolution numerical models of tropical cyclones is recommended to better understand these processes.

This paper has dealt with composite (and thus essentially azimuthally-averaged) fields. The tropical cyclone outflow layer tends to be organized into individual outflow channels (Rappin et al. 2011; Merrill and Velden 1996). These are analogous to maxima in poleward flow of low potential vorticity air at localized longitudes in the Hadley Cell studied by Sato and Dunkerton (2002). Future work will address such asymmetric features in the tropical cyclone.

Acknowledgements. We thank Drs. Tim Dunkerton of Northwest Research Associates and David Nolan of the University of Miami for helpful discussions of this work. Dr. Nolan also provided

the data for Figure 6 of this paper. We appreciate the careful reading of the manuscript by three anonymous reviewers. G-IV dropsonde data were obtained from the Hurricane Research Division of NOAA. ERA Interim analyses were obtained from the National Center for Atmospheric Research, which is supported by the National Science Foundation (NSF). This paper was supported by NSF Grant AGS1132576 and Office of Naval Research Grant N000141410162.

REFERENCES

Alaka, M.A., 1962: On the occurrence of dynamic instability in incipient and developing hurricanes. *Mon. Wea. Rev.*, **90**, 49-58.

Anthes, R.A., 1972: Development of asymmetries in a three-dimensional numerical model of the tropical cyclone. *Mon. Wea. Rev.*, **100**, 461-476.

Black, P.G., and R.A. Anthes, 1971: On the asymmetric structure of the tropical cyclone outflow layer. *J. Atmos. Sci.*, **28**, 1348-1366.

Bu, Y.P., R. Fovell, and K.L. Corbosiero, 2014: Influence of cloud-radiative forcing on tropical cyclone structure. *J. Atmos. Sci.*, in press.

Bui, H.H., R.K. Smith, M.T. Montgomery, and J. Peng, 2009: Balanced and unbalanced aspects of tropical-cyclone intensification. *Quart. J. Roy. Meteor. Soc.*, **135**, 1715-1731.

Cairo, F., C. Buontempo, A.R. MacKenzie, C. Schiller, C.M. Volk, A. Adriani, V. Mitev, R. Matthey, G. DiDonfrancesco, A. Oulanovksy, F. Ravegnani, V. Yushkov, M. Snels, C. Cagnazzo, and L. Stefanutti, 2008: Morphology of the tropopause layer and lower stratosphere above a tropical cyclone: a case study on cyclone Davina (1999). *Atmos. Chem. Phys*., **10**, 3411-3426.

Chen, H., and D.-L. Zhang, 2013: On the rapid intensification of Hurricane Wilma (2005). Part II: Convective bursts and the upper-level warm core. *J. Atmos. Sci.*, **70**, 146-162.

Emanuel, K.A., 1983: The Lagrangian parcel dynamics of moist symmetric instability. *J. Atmos. Sci.*, **40**, 2368-2376.

Franklin, J.L., R.J. Pasch, L.A. Avila, J.L. Beven, M.B. Lawrence, S.R. Stewart, and E.S. Blake, 2006: Atlantic hurricane season of 2004. *Mon. Wea. Rev.*, **134**, 981-1025.

Held, I.M., and A.Y. Hou, 1980: Nonlinear axially symmetric circulations in a nearly inviscid atmosphere. *J. Atmos. Sci.*, **37**, 515-533.

Hock, T.F., and J.L. Franklin, 1999: The NCAR GPS Dropsonde. *Bull. Amer. Meteor. Soc.*, **80**, 407-420.

Huang, Y.-H., M. T. Montgomery, and C.-C. Wu, 2012: Concentric eyewall formation in Typhoon Sinlaku (2008) - Part II: Axisymmetric dynamical processes. *J. Atmos. Sci.*, **69**, 662-674.

Kepert, J.D., 2010: Tropical cyclone structure and dynamics. In *Global Perspectives on Tropical Cyclones*, World Scientific Publishing, 3-54.

Kleinschmidt, E., 1951: Grundlagen einer Theorie der tropischen Zyklonen. *Archiv. Meteor., Geophys., Bioklim.A*, **4**, 53-72.

Melhauser, C., and F. Zhang, 2014: Diurnal radiation cycle impact on the pregenesis environment of Hurricane Karl (2010). *J. Atmos. Sci.*, **71**, 1241-1259.

Merrill, R.T., and C.S. Velden, 1996: A three-dimensional analysis of the outflow layer of Supertyphoon Flo (1990). *Mon. Wea. Rev.*, **124**, 47-63.

Molinari, J., P. Duran, and D. Vollaro, 2014: Low Richardson number in the tropical cyclone outflow layer. *J. Atmos. Sci*, in press.

Molinari, J., D.M. Romps, D. Vollaro, and L. Nguyen, 2012: CAPE in tropical cyclones. *J. Atmos. Sci.*, **69**, 2452-2463.

Möller, J.D., and L.J. Shapiro, 2002: Balanced contributions to the intensification of Hurricane Opal as diagnosed from a GFDL model forecast. *Mon. Wea. Rev.*, **130**, 1866-1881.

Nolan, D.S., R. Atlas, K.T. Bhatia, and L.R. Bucci, 2013: Development and validation of a hurricane nature run using the joint OSSE nature run and the WRF model. *J. Adv.Modeling Earth Sys.*, **5**, 382-405.

Ooyama, K., 1966: On the stability of the baroclinic circular vortex: A sufficient condition for instability. *J. Atmos. Sci.*, **23**, 43-53.

Ooyama, K., 1969: Numerical simulation of the life cycle of tropical cyclones. *J. Atmos. Sci.*, **26**, 3-40.

Rappin, E.D., M.C. Morgan, and G.J. Tripoli, 2011: The impact of outflow environment on tropical cyclone intensification and structure. *J. Atmos. Sci.*, **68**, 177-194.

Sato, K., and T.J. Dunkerton, 2002: Layered structure associated with low potential vorticity near the tropopause seen in high-resolution rawinsondes over Japan. *J. Atmos. Sci.*, **59**, 2782-2800.

Sawyer, J.S., 1947: Notes on the theory of tropical cyclones. *Quart. J. Roy. Meteor. Soc.*, **73**, 101-126.

Sitkowski, M., J.P. Kossin, and C.M. Rozoff, 2011: Intensity and structure changes during hurricane eyewall replacement cycles. *Mon. Wea. Rev.*, **139**, 3829–3847.

Thorpe, A.J., B.J. Hoskins, and V. Innocentini, 1989: The parcel method in a baroclinic atmosphere. *J. Atmos. Sci.*, **46**, 1274-1284.

Wirth, V., and T.J. Dunkerton, 2006: A unified perspective on the dynamics of axisymmetric hurricanes and monsoons. *J. Atmos. Sci.*, **63**, 2529-2547.

Yanai, M., 1964: Formation of tropical cyclones. *Rev. Geophys.*, **2**, 367-414.

Table 1. Mean sonde release time versus radius and its standard deviation over the 10 days of G-IV flights. Also shown is the number of sondes for each 100-km radial bin.

RADIUS RANGE (KM)	MEAN SONDE RELEASE TIME (NEAREST HOUR)	STANDARD DEVIATION (HOURS)	NUMBER OF SONDES
100-200	1400 UTC 11 SEPTEMBER	68	15
200-300	0700 UTC 12 SEPTEMBER	64	40
300-400	1800 UTC 12 SEPTEMBER	58	46
400-500	0000 UTC 12 SEPTEMBER	66	54
500-600	0000 UTC 12 SEPTEMBER	68	37

FIGURE LEGENDS

Figure 1. Distribution of sonde release locations with respect to the center of Hurricane Ivan during the period 6-16 September 2004.

Figure 2. Radial-vertical cross-section of mean absolute angular momentum from Eq. 1 (increment: 7.5 X 10^5 m^2 s^{-1}) in 100-km radial and 100-m vertical resolution. Stippling indicates the region where *M* decreased outward.

Figure 3. (a) Radial-vertical cross-section of mean storm-relative radial velocity (increment 1 m s^{-1}). Blue: inflow; yellow: outflow; dark yellow: outflow > 4 m s^{-1}. (b) Same, but for storm-relative tangential velocity (increment 3 m s^{-1}). Blue: cyclonic flow; yellow: anticyclonic. Points A and A' in Fig. 3a will be discussed with later figures.

Figure 4. Radial-vertical cross-section of mean absolute angular momentum (contoured) as in Fig 2, plotted over mean relative humidity (per cent; shaded). Red stippling indicates the region where absolute angular momentum decreases outward. The small unshaded area top left indicates a lack of relative humidity observations. The significance of point A is discussed later in tandem with Fig. 5(a,b).

Figure 5. (a) Mean absolute angular momentum as in Fig. 4, plotted with equivalent potential temperature θ_e (shaded with dashed line increment 1 K). (b) As in (a), but with θ_v replacing θ_e. Blue stippling represents regions of (a) moist and (b) dry symmetric instability. Points A, A', and B are discussed in the text.

Figure 6. (a) Azimuthally averaged absolute angular momentum (dark black contours; increment 10 X 10^5 m^2 s^{-1}) and equivalent potential temperature (θ_e; shaded) from the hurricane nature run of Nolan et al. (2013), valid at 1500 UTC 3 August. The blue stippling indicates the region of

inertial instability, which is nearly identical to that for moist symmetric instability. (b) As in (a), but for a 48-hour mean beginning 0000 UTC 3 August.

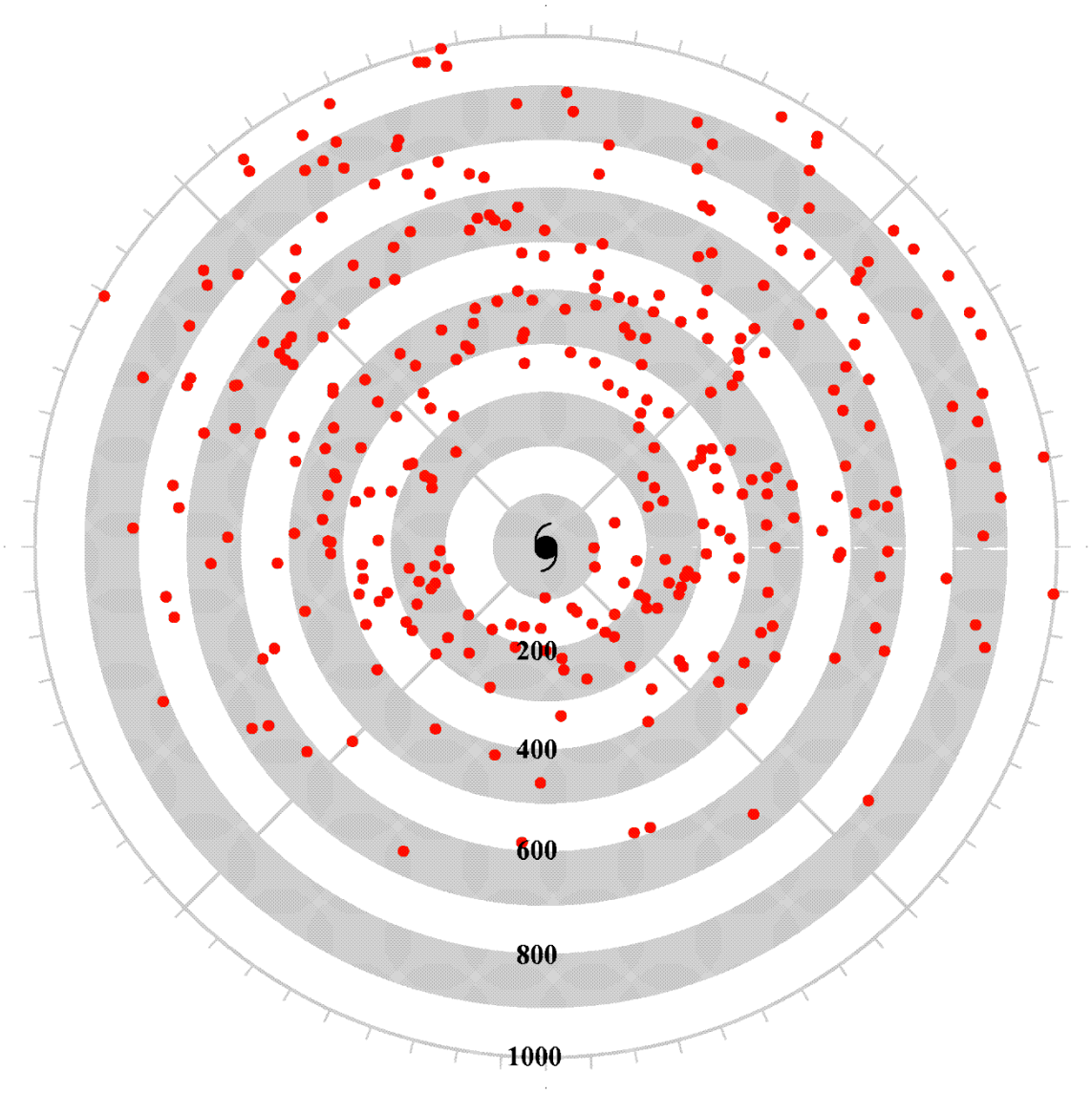

Figure 1. Distribution of sonde release locations with respect to the center of Hurricane Ivan during the period 6-16 September 2004.

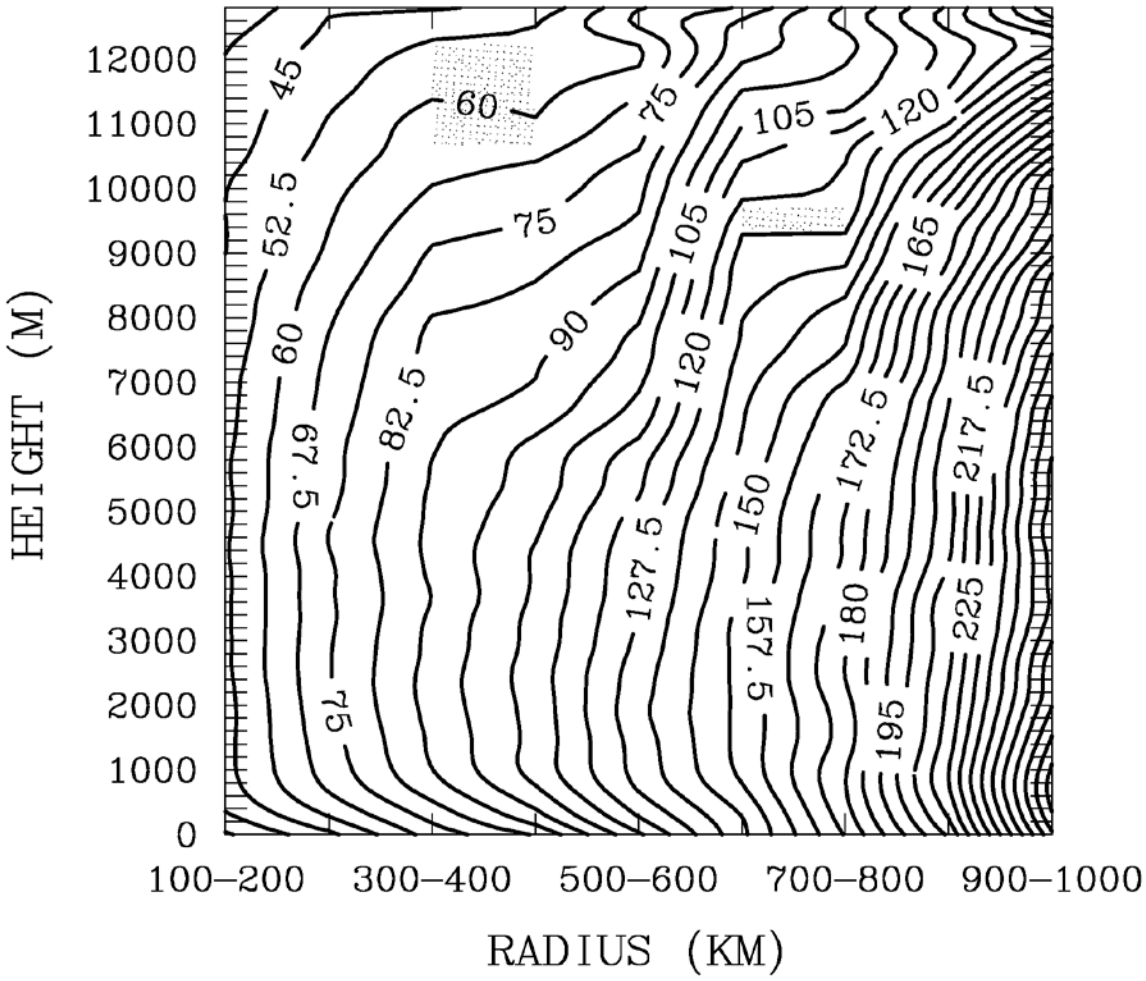

Figure 2. Radial-vertical cross-section of mean absolute angular momentum from Eq. 1 (increment: 7.5 X 10^5 m^2 s^{-1}) in 100-km radial and 100-m vertical resolution. Stippling indicates the region where *M* decreased outward.

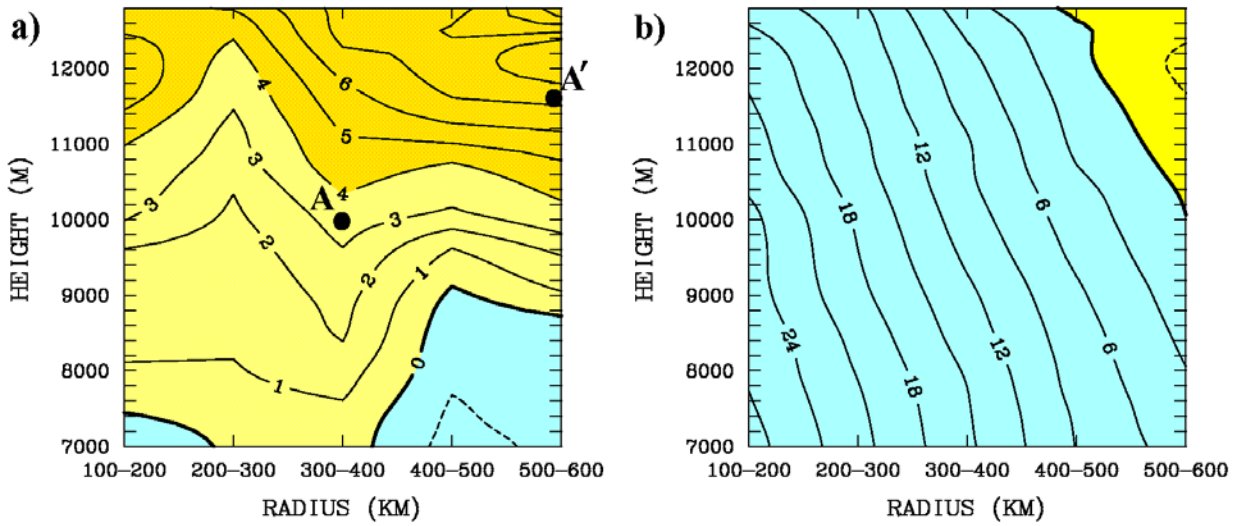

Figure 3. (a) Radial-vertical cross-section of mean storm-relative radial velocity (increment 1 m s^{-1}). Blue: inflow; yellow: outflow; dark yellow: outflow > 4 m s^{-1}. (b) Same, but for storm-relative tangential velocity (increment 3 m s^{-1}). Blue: cyclonic flow; yellow: anticyclonic. Points A and A' in Fig. 3a will be discussed with later figures.

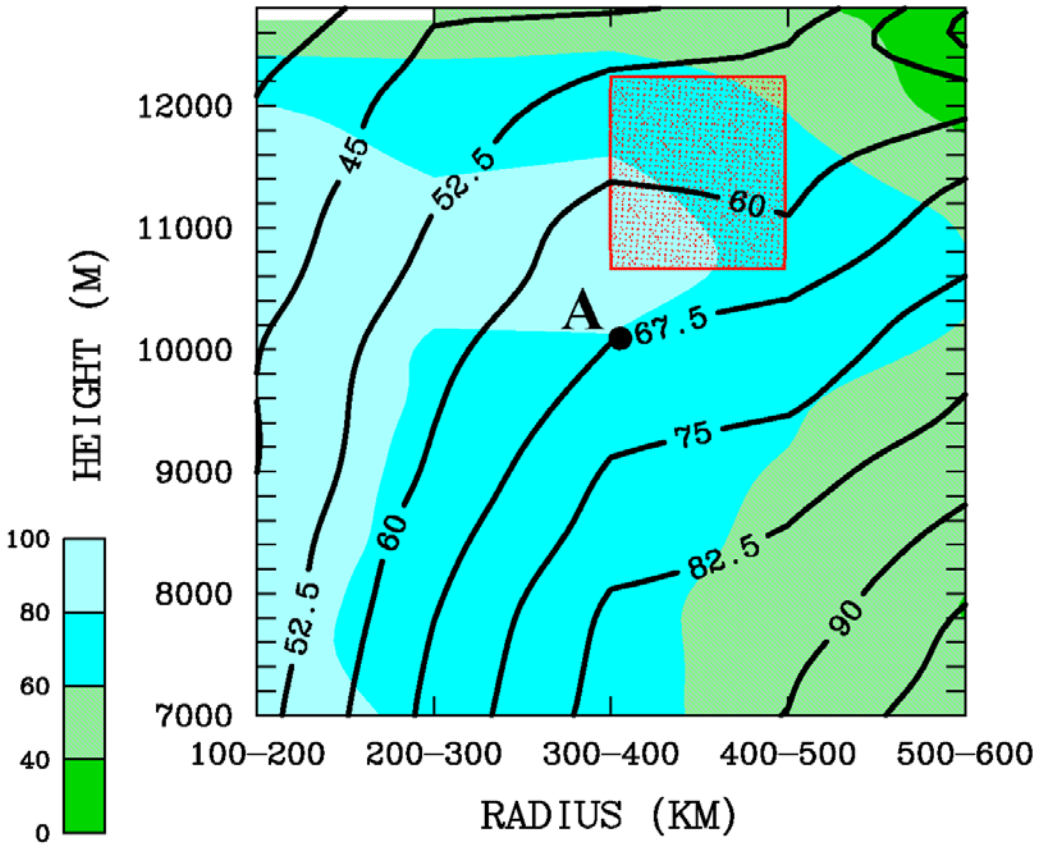

Figure 4. Radial-vertical cross-section of mean absolute angular momentum (contoured) as in Fig 2, plotted over mean relative humidity (per cent; shaded). Red stippling indicates the region where absolute angular momentum decreases outward. The small unshaded area top left indicates a lack of relative humidity observations. The significance of point A is discussed later in tandem with Fig. 5(a,b).

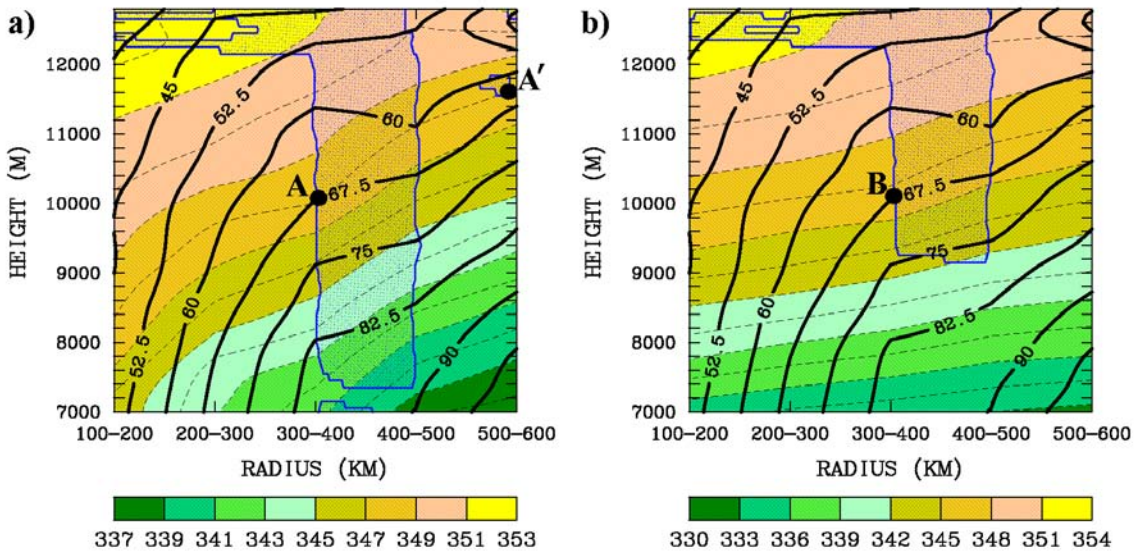

Figure 5. (a) Mean absolute angular momentum as in Fig. 4, plotted with equivalent potential temperature θ_e (shaded with dashed line increment 1 K). (b) As in (a), but with θ_v replacing θ_e. Blue stippling represents regions of (a) moist and (b) dry symmetric instability. Points A, A', and B are discussed in the text.

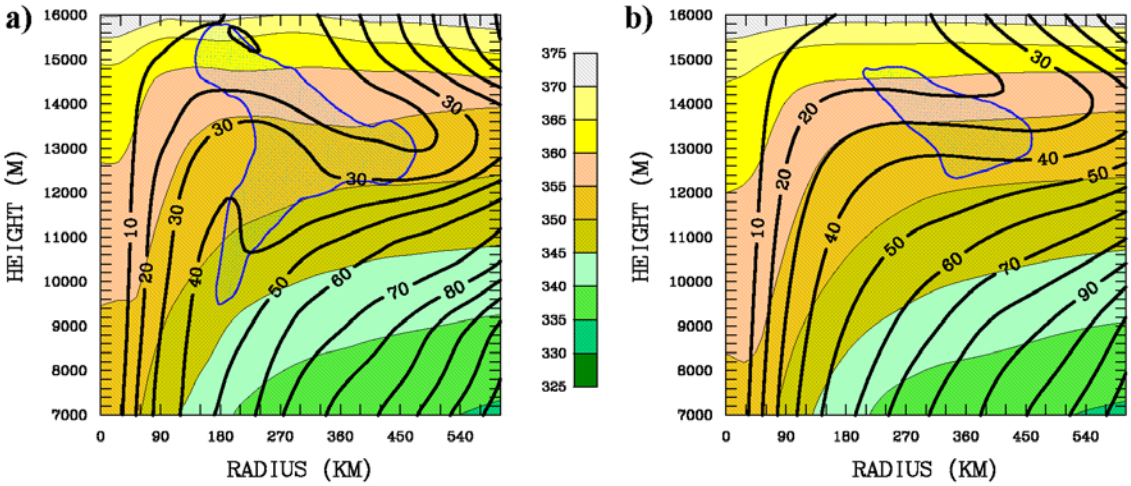

Figure 6. (a) Azimuthally averaged absolute angular momentum (dark black contours; increment 10 X 10^5 m^2 s^{-1}) and equivalent potential temperature (θ_e; shaded) from the hurricane nature run of Nolan et al. (2013), valid at 1500 UTC 3 August. The blue stippling indicates the region of inertial instability, which is nearly identical to that for moist symmetric instability. (b) As in (a), but for a 48-hour mean beginning 0000 UTC 3 August.